Materials Today Physics 32 (2023) 101012

Contents lists available at ScienceDirect

Materials Today Physics

journal homepage: www.journals.elsevier.com/materials-today-physics

Unlocking the potential of hexagonal boron sheets: Giant improvements in thermal conductivity and mechanics through molybdenum intercalation

Mohammad Alidoosti [a], Davoud Nasr Esfahani [a,b,*], Shahram Yalameha [c], Daryoosh Vashaee [d,**]

[a] Pasargad Institute for Advanced Innovative Solutions (PIAIS), Tehran, 19916-33361, Iran
[b] Department of Converging Technologies, Khatam University, Tehran, 19916-33357, Iran
[c] Faculty of Physics, University of Isfahan, Isfahan, 81746-73441, Iran
[d] Department of Electrical and Computer Engineering, North Carolina State University, Raleigh, NC, 27606, USA

ARTICLE INFO

Keywords:
Lattice thermal conductivity
Mechanical properties
Molybdenum tetra-borides

ABSTRACT

A new two-dimensional (2D) material, MoB_4, known as a Dirac material, has been found to possess exceptional electronic properties and promising thermal and mechanical characteristics. Our calculations reveal that MoB_4 has a remarkable Young's modulus of 384 N/m, surpassing that of graphene. Additionally, we predict that MoB_4 exhibits a thermal conductivity of 461 W/mK at room temperature. This is a significant improvement when compared to a single boron sheet in a honeycomb structure and MoB_2, showing 32 and 8 times higher thermal conductivity, respectively. This enhancement in thermal conductivity is attributed to the suppression of anharmonicity and scattering phase space, along with an increased group velocity in MoB_4.

1. Introduction

Transition metal borides (TMBs) have attracted much attention in various fields, where a few examples are MgB_2 for superconductivity, TiB_2 for mechanical toughness, or WB_4 as a superhard material [1–5] for which hardness of ~ 46 GPa has been reported in a bulk configuration [6]. Heavy TMs can emerge with such stiffness when bonded with light atoms like B and C [7–9], via a charge transfer mechanism from the TM to the light atom that can lead to three types of bonds, namely, covalent, ionic, and metallic [10].

Borophene has been successfully synthesized through micro-mechanical exfoliation [11] with remarkable electronic and mechanical properties [11,12]. Although boron cannot form a graphene-like monolayer due to electron deficiency [13,14], it could be stabilized with strain and induction of extra electrons [14]. In this regard, hexagonal boron monolayer could be realized by sandwiching TMs such as Mo and W within two hexagonal boron monolayers which could compensate for the electron deficiency through charge transfer into boron sheets and eventually gives rise to dynamically and thermodynamically stable phases of 2D TMB_x [15–19]. In this line, tungsten and molybdenum tetra-borides are initial promising candidates to scrutinize as superhard materials. Compared to B–W, more boron concentration alongside B–B covalent bonds and short, strong, B–Mo bonds could lead to a more rigid structure like MoB_4. Moreover, beyond typical Dirac-like electronic band structures (e.g., graphene), the band structure of molybdenum tetra-borides contains twelve Dirac cones in the 1st Brillouin zone, including the six cones at the high symmetry point K and others at the middle of Γ-K path [20,21]. The Dirac cones in these materials make them promising candidates for high-performance electronic applications due to their very high Fermi velocity [20].

The work of Xie et al. in Ref. [15] focused on the electronic structure properties of 2D MoB_4, however, the mechanical and phononic properties were not investigated. This present study aims to fill this gap by addressing the mechanical and phononic properties of MoB_4. As mentioned earlier, MoB_4 passes the initial checks for promising 2D superhard materials; consequently, a high lattice thermal conductivity (κ_{ph}) is expected. Nowadays, materials with high enough κ_{ph} could be invoked as fillers in electronic nano-devices for thermal dissipation [22].

MoB_4 is composed of two boron sheets and one Mo sheet; therefore, it is a good practice to compare the thermal conductivity of MoB_4 to that of its constituents. In this context, there are several other efforts to improve the thermal conductivity of boron sheets; for instance, it was shown that the intercalation of Al atoms into bilayer δ_4 borophene results in a three-fold enhancement of thermal conductivity (κ_{ph} ~ 160 W/mK;

* Corresponding author. Pasargad Institute for Advanced Innovative Solutions (PIAIS), Tehran, 19916-33361, Iran.
** Corresponding author.
E-mail addresses: dd.nasr@gmail.com (D.N. Esfahani), dvashae@ncsu.edu (D. Vashaee).

https://doi.org/10.1016/j.mtphys.2023.101012
Received 26 November 2022; Received in revised form 16 January 2023; Accepted 9 February 2023
Available online 11 February 2023

considering 3.60 Å as an effective thickness) in armchair direction at room temperature (RT) [23]. Additionally, previous studies have reported that hydrogenated bilayer honeycomb boron arsenide exhibits in-plane thermal conductivity of approximately 313 W/mK (when considering an effective thickness of 8.11 Å) at RT [24]. However, this value is reduced by approximately ~30% when four-phonon scattering is taken into account [25].

Comparing the latter with a single hexagonal boron sheet (stabilized through electron doping or strain, $\kappa_{ph} = 14.2$ W/mK), we observe a 22-fold enhancement of the in-plane thermal conductivity in boron arsenide [14]. It is worth noting that while a single-layer honeycomb boron sheet maintains σ_h symmetry, its thermal conductivity is relatively low when compared to some carbon-based materials [26–28], and, on the other hand, is close to what was reported in Ref. [29]. Recently, single layer MoB_2 was shown to be dynamically stable, with an estimated thermal conductivity of $\kappa_{ph} = 36$ W/mK (rescaled to our effective thickness of 6.33 Å) by accepting minor artificial negative frequencies of ZA mode close to the zone center [30], while our results, without any sign of negative frequencies, show $\kappa_{ph} = 60$ W/mK. MoB_4 is the result of adding another honeycomb boron sheet to the Mo sheet such that the resulting structure preserves σ_h symmetry. Based on first-principles calculations, we show that such a modification gives rise to a significant thermal conductivity enhancement compared to MoB_2 and a single graphene-like boron sheet. To this end, our calculations show approximately 32 and 8 times thermal conductivity enhancement compared to a single honeycomb boron sheet and MoB_2, respectively. MoB_4 shows comparable thermal and better mechanical properties than graphene. Our results indicate that the thermal conductivity of MoB_4 has a smaller contribution from the ZA modes, when compared to that of graphene.

2. Theory and computational details

First-principles calculations are performed within the density functional theory (DFT) framework implemented in QUANTUM ESPRESSO distribution [31]. Our calculations were carried out using the PAW/PBE pseudopotential [32]. Both in-plane atomic positions and lattice constants were relaxed until all forces and the pressure were less than $10^{-5}\ eV/\mathring{A}$ and 0.5 kbar, respectively. A kinetic cut-off of 50 Ry is used for the Kohn-sham wave functions, while 400 Ry is considered for the density cut-off. A $24 \times 24 \times 1$ **k**-point grid was applied for electronic integration with Monkhorst-Pack mesh [33]. To eliminate spurious interaction between adjacent layers, a vacuum space of 20 Å along the *z*-direction was adopted. To compute the phonon frequencies and electron-phonon matrix elements of the system, the density functional perturbation theory (DFPT) with the self-consistency threshold of 1×10^{-16} Ry was applied [34].

To calculate the lattice thermal conductivity, κ_{ph}, of 2D MoB_4, anharmonic third-order interatomic force constants (IFCs) are needed, accompanied by second-order IFCs extracted from DFPT [34]. In our calculations, we have considered 3^{rd}IFCs up to the fourth shell of neighbors [35] in a $5 \times 5 \times 1$ supercell and $3 \times 3 \times 1$ **k**-mesh, while a fine mesh $160 \times 160 \times 1$ is adopted in Fourier transformation in **q**-space accompanied with scalbroad 1.0. We calculate the thermal conductivity of 2D MoB_4 by solving the phonon BTE with an iterative self-consistent algorithm as implemented in the ShengBTE package [36–38]. Intrinsic three phonon scattering processes have been considered in the calculation of phonon relaxation times (τ_λ):

$$\frac{1}{\tau_\lambda} = \frac{1}{N}\left(\sum_{\lambda'\lambda''}^{+}\Gamma^{+}_{\lambda\lambda'\lambda''} + \frac{1}{2}\sum_{\lambda'\lambda''}^{-}\Gamma^{-}_{\lambda\lambda'\lambda''} + \sum_{\lambda'}\Gamma^{ext}_{\lambda\lambda'}\right), \tag{1}$$

where N is the number of **q** points in the Brillouin zone, $\Gamma^{+}_{\lambda\lambda'\lambda''}$ and $\Gamma^{-}_{\lambda\lambda'\lambda''}$ represent the scattering rates due to absorbing and emitting three-phonon processes, respectively. The extrinsic scattering term $\Gamma^{ext}_{\lambda\lambda'}$ comprises isotopic disorder. Next, the lattice thermal conductivity tensor is expressed as:

$$\kappa^{\alpha\beta} = \frac{1}{V}\sum_{\lambda}\hbar\omega_\lambda\frac{\partial n}{\partial T}v^{\alpha}_{\lambda}v^{\beta}_{\lambda}\tau_\lambda, \tag{2}$$

where V is the volume of the unit cell, n is the Bose-Einstein distribution function, v^{α}_{λ} is the group velocity, and ω_λ is phonon frequency. λ index embraces both phonon **q** vectors and branch numbers.

Following Ref. [39], the lattice thermal expansion, α, can be calculated using,

$$\alpha = \frac{1}{a_0^2\frac{\partial E^2}{\partial a^2}}\sum_{q,\nu}c_v(q,\nu)\widetilde{\gamma}_{q,\nu}, \tag{3}$$

where $c_v(q,\nu) = k_B\frac{x^2}{\sinh^2 x}$, $x = \frac{\hbar\omega}{2k_BT}$ and $\widetilde{\gamma}_{q,\nu} = -\frac{a_0}{\omega_{q,\nu}}\frac{d\omega_{q,\nu}}{da}|_{a=a_0}$. Assuming that the variation of phonon frequencies is insignificant compared to the variation of volume in the z-direction (perpendicular to the direction of the 2D plane, which includes a large enough vacuum to prevent interaction between repeated images), we have $\gamma_{q,\nu} = -\frac{V_0}{\omega_{q,\nu}}\frac{d\omega_{q,\nu}}{dV}|_{V=V_0} = -\frac{S_0}{\omega_{q,\nu}}\frac{d\omega_{q,\nu}}{dS}|_{S=S_0}$. Considering $S_0 = \frac{\sqrt{3}}{2}a_0^2$ for our case, the relation between $\gamma_{q,\nu}$ and $\widetilde{\gamma}_{q,\nu}$ becomes $\widetilde{\gamma}_{q,\nu} = 2\gamma_{q,\nu}$. Inserting back this result into Eq. (3), we have,

$$\alpha = \frac{2}{a_0^2\frac{\partial E^2}{\partial a^2}}\sum_{q,\nu}c_v(q,\nu)\gamma_{q,\nu}. \tag{4}$$

$\frac{\partial E^2}{\partial a^2}$ is calculated by fitting a quadratic polynomial into the total energy data. The total energy is evaluated for 11 points of bi-axial strain from −2.5% to +2.5% of a_0 (equilibrium lattice constant) and with a step length of 0.5%.

To calculate elastic constants in 2D materials, we employ Hooke's law under plane-stress condition [40] as follows:

$$\begin{bmatrix}\sigma_{11}\\ \sigma_{22}\\ \sigma_{12}\end{bmatrix} = \begin{bmatrix}C_{11} & C_{12} & 0\\ C_{21} & C_{22} & 0\\ 0 & 0 & C_{66}\end{bmatrix}\begin{bmatrix}\epsilon_{11}\\ \epsilon_{22}\\ 2\epsilon_{12}\end{bmatrix}. \tag{5}$$

In the energy approach, similar to 3D materials, the elastic stiffness constants of 2D materials can be calculated using the equation [41],

$$C_{ij} = \frac{1}{S_0}\frac{\partial^2 E}{\partial\epsilon_i\partial\epsilon_j}, \tag{6}$$

where E and S_0 are the energy and area of the simulation cell in the *x*-*y* plane (usually the equilibrium one), respectively. In addition, $\frac{\partial^2 E}{\partial\epsilon_i\partial\epsilon_j}$ is the second derivative of the strain energy with respect to the uniaxial strain. In this work, the uniaxial strains in the range of $\varepsilon = -6\%$ to $\varepsilon = 6\%$ with a step of 2% are applied to two in-plane directions. The negative and positive values of this range indicate the compressive strain and tensile strain, respectively. Under each strain, the ionic positions of the 2D MoB_4 structures are fully relaxed. Finally, we obtain the in-plane elastic constant by the polynomial fitting of the strain-dependent energy values [42]. The elastic constants were calculated using the IRELAST2D code [41] based on the energy approach. These calculations were carried out within the full-potential augmented plane-wave + local orbitals method, encoded in the WIEN2K package [43]. In addition, mechanical properties were analyzed using the ELATOOLS code as well [44].

3. Numerical results and discussions

3.1. General properties

The relaxed geometry of the MoB_4 monolayer showed an optimized hexagonal unit cell with D_{6h} symmetry consisting of two boron layers embracing a triangle lattice of Mo atoms in their interval space, as

depicted in Fig. 1(a). Such a structure is dynamically stable and preserves σ_h symmetry. Our results show that the optimal lattice parameter $a = 2.96$ Å and covalently bonded B–B and ionic-covalent bonded B–Mo lengths are 1.71 and 2.37 Å, respectively. In comparison, the two boron layers are separated by distance $d_{B\text{-}B} = 3.28$ Å, which has good agreement with Ref. [15]. Bader charge analysis implemented in Critic2 [45,46] indicates such a strong bond arises from the transfer of slightly more than 1 *e/cell* from Mo atom to the adjacent B atoms.

In 2D structures, an effective thickness is required to determine the thermal conductivity and mechanical properties, which is often considered a Van der Waals (VdW) diameter between the two isolated layers of the material. In this work, the effective thickness of about 6.33 Å is estimated when grimme-d2 as a VdW correction was employed. The electronic band structure of monolayer MoB_4 is shown in Fig. 1(b), consisting of two Dirac points at K and between K and Γ illustrated in the inset of this figure as well. Our calculations disclose that the ground state of this structure is nonmagnetic metal with weak spin-orbit effects neglected in this work due to having no effects on the crystal structure and mechanical or thermal properties. Spin-orbit effects can open a gap of about 40 meV at Dirac cones; however, the system remains metallic, as demonstrated in Fig. 1(b).

3.2. Mechanical properties

We calculated the in-plane elastic constants to evaluate the mechanical stability of the MoB_4 monolayer. The hexagonal structure of this monolayer possesses two independent second-order elastic constants, C_{11} and C_{12} ($C_{66} = (C_{11}–C_{12})/2$). The mechanical stability is evaluated by Born's stability criteria [47,48] as $C_{11}–C_{12} > 0$ and $C_{11} + C_{12} > 0$. The obtained elastic constants in Table 1 meet the elastic stability criteria for MoB_4. To further examine the mechanical behavior of this monolayer, we investigate its mechanical properties, including Young's modulus (E) and Poisson's ratio (ν) listed in Table 1. This table shows Young's modulus is 383.8 N/m, which is interestingly larger than graphene (348 N/m) [49], α-borophene (210 N/m), β_{12}-borophene (203 N/m) and borophane (172 N/m) [50,51]. It is also 31.9% and 46.6% larger than penta-graphene (268 N/m) [52] and Me-graphene (210 N/m) [53], respectively. The Poisson's ratio can be defined as a C_{12}/C_{11}, which is 0.159 for this structure (see Table 1), slightly different from MoB_2 (0.196), graphene (0.169), α-borophene (0.196), β_{12}-borophene (0.199) and borophane (0.177) [50,51]. We calculate the direction-dependent Young's modulus and Poisson's ratio to check for the isotropic or anisotropic mechanical behavior in MoB_4. The results show Young's modulus and Poisson's ratio of this monolayer are isotropic.

3.3. Lattice thermal conductivity

The phonon dispersion of monolayer MoB_4 and band resolved Grüneisen parameters (γ) are shown in Fig. 2(a). Moreover, the type of σ_h symmetry in this material differs from that of graphene, i.e., boron atoms lay away from the σ_h plane, thus differing from purely single-layer flat materials such as graphene. In this case, the in-plane and ZA distortions couple, resulting in slight linear dispersion for the ZA mode of MoB_4. Moreover, such coupling appears to suppress the softening of ZA mode compared to graphene.

The mode-dependent Grüneisen parameters play a crucial role in determining thermal expansion mechanisms. Moreover, it is an indicator of the magnitude of anharmonicity. As depicted in Fig. 2(a), these mode-resolved parameters are generally positive for almost all branches in a wide range of **q** vectors but are slightly negative for small **q** ones close to the zone center relevant to ZA mode. Compared with other 2D materials such as graphene, germanene, and blue phosphorene, the magnitude of Grüneisen parameter corresponding to ZA is much smaller [54]. This is further supported by the behavior of the total Grüneisen parameter, which becomes negative only below 66 K as shown in the lower right inset of Fig. 2(b), resulting in a negative thermal expansion coefficient (TEC) below this temperature as illustrated in the upper left inset of Fig. 2(b). Additionally, our results indicate that the TEC of a monolayer of MoB_4 is approximately 3.5×10^{-6} K^{-1} at 300 K (see Fig. 2 (b)).

To better understand the thermal properties of MoB_4, it is helpful to perform an analysis composed of a detailed comparison of various aspects of the κ_{ph} with other 2D boron compounds. The first candidate can be the hexagonal boron sheet; however, since a single-layer boron sheet is only stable under large doping or strain, we chose another boron compound MoB_2 composed of a hexagonal Mo covered with a hexagonal boron sheet [30]. Our results here agree well with the ones in Ref. [30]. However, it should be noted that our results for κ_{ph} of MoB_2 are reported for an effective Van der Waals diameter of 6.33 Å, which was not considered in Ref. [30].

In Table 1, the sound velocities of in-plane modes of MoB_4 and MoB_2 are compared, indicating that they are both approximately isotropic. Moreover, MoB_4 sound velocities are 30% larger than MoB_2. Thus a

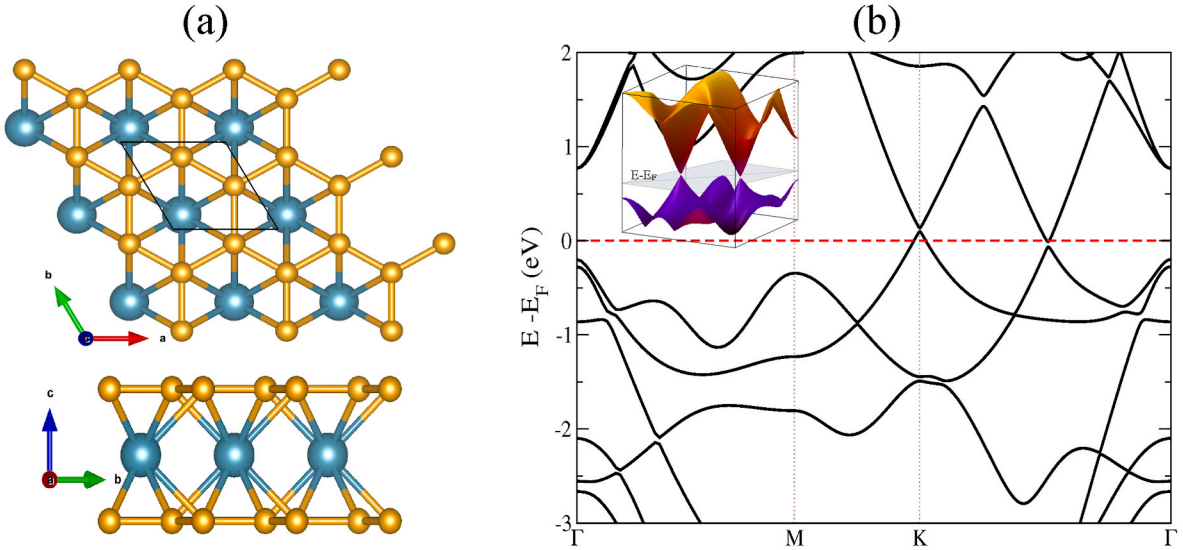

Fig. 1. (a) Top and side views of MoB_4 monolayer. (b) The electronic band structure of MoB_4 monolayer along the high symmetry path by considering the spin-orbit effect. The inset shows a 3D representation of the two Dirac cones. The blue and orange refer to Mo and B atoms, respectively.

Table 1
Elastic constants C_{ij} (N/m), Young's modulus (E), and Poisson's ratio (ν) alongside group velocity, V (km/s), of MoB_4 compared to MoB_2 along the high symmetry path. The amounts in the parentheses have been taken from Ref. [30].

	Elastic constants					$V^{\Gamma-M}$		$V^{\Gamma-K}$	
	C_{11}	C_{12}	C_{66}	E	ν	TA	LA	TA	LA
MoB_4	393.7	62.6	165.6	383.8	0.159	8.8	12.3	8.3	11.7
MoB_2	235.2 (225.8)	46.2 (51.3)	94.5 (87.2)	226.1 (214.1)	0.196 (0.23)	5.9	9.1	5.9	9.2

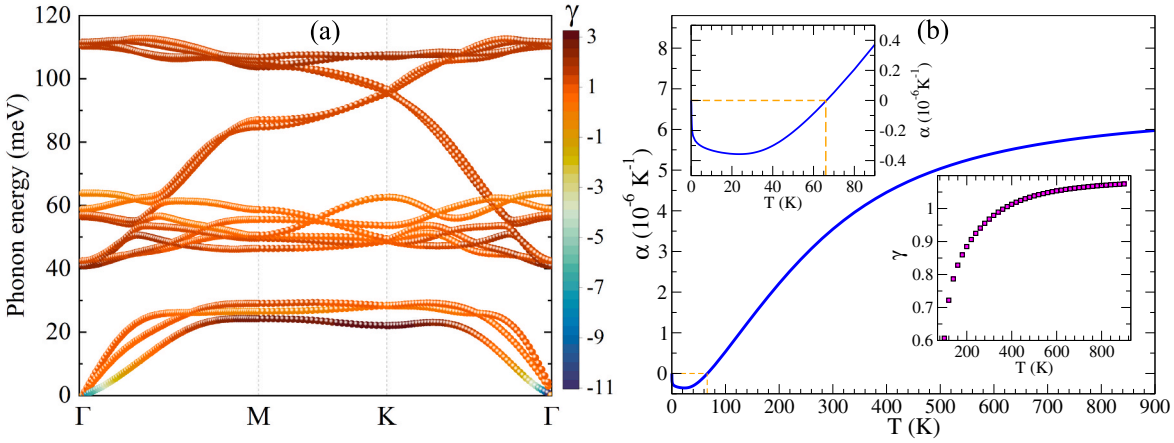

Fig. 2. (a) The momentum-resolved Grüneisen parameter (γ) mapped on the phonon dispersion along the high symmetry path. (b) The lattice thermal expansion (α) of a MoB_4 monolayer as a function of temperature. The upper left inset shows a zoomed-in view of thermal expansion in the range of 1–90 K. The lower right inset displays the Grüneisen parameter versus temperature.

larger thermal conductivity is expected for MoB_4 in comparison with MoB_2.

Fig. 3 (a) shows the thermal conductivity of MoB_2 and MoB_4 as a function of temperature. MoB_4 shows larger thermal conductivity in the whole range of temperatures than MoB_2. The results show that κ_{ph} yields 461 (60) W/mK for MoB_4 (MoB_2) comparable with what was reported for α-borophene (~ 14 W/mK) [55], monolayer β_{12}-borophene (~ 90 W/mK) and bilayer β_{12}-borophene (140.5 W/mK) [56,57] at RT. The contributions of the most important modes to the κ_{ph} are also shown in the inset of Fig. 3(a), indicating almost the same pattern for both systems. Compared to graphene as a single atomic layer with σ_h symmetry, MoB_4 preserves σ_h symmetry as well, and the share of ZA mode in the κ_{ph} of MoB_4 (35%) is interestingly much smaller than that of graphene (75%) [26] as illustrated in the inset of Fig. 3. The main reason for this reduction is that the scattering channels with odd ZA deformations are forbidden for graphene. However, due to the type σ_h symmetry in MoB_4, where there are atoms away from the σ_h symmetry plane, such a condition does not hold; hence, the scattering channels with an odd number of ZA mode deformations are active [58] for these types of structures. Besides, such a discrepancy between graphene and MoB_4 symmetries arising from their configurations (purely-2D vs. quasi-2D) manifests itself in the electron-phonon interactions [59]. In addition, more details express that increasing the temperature reduces (increases) the ZA (LA) mode contribution of κ_{ph} to 32% (34%). In contrast, the dominant contribution of ZA phonons for graphene remains even at high temperatures [60]. Notice that optical contributions appear only at T> 500 K for graphene [26]. In comparison with materials with broken σ_h symmetry, the presence of σ_h in materials like MoB_4 still imposes a

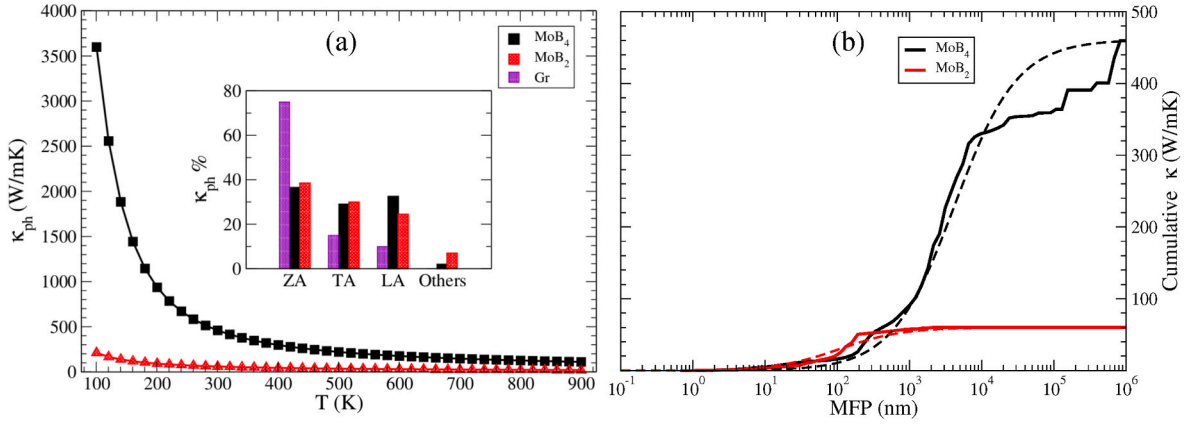

Fig. 3. (a) The calculated lattice thermal conductivity, κ_{ph}, of MoB_4 and MoB_2 monolayer as a function of temperature. The inset displays the percent contribution of the various acoustic and optical branches in forming κ_{ph}. At RT, κ_{ph} is 461 and 60 (W/mK) for MoB_4 and MoB_2, respectively. The results related to graphene are taken from Ref. [26] (b) Cumulative lattice thermal conductivity of MoB_4 and MoB_2 as a function of the maximum mean free path (MFP) at 300 K. An effective layer thickness tantamount to 6.33 Å has been considered.

constraint on the selection rule of scattering matrix elements $\Gamma_{\lambda\lambda'\lambda''}$. That is, all of the scattering channels with pure Mo deformations with an odd number of ZA deformations are forbidden in MoB_4, while such scattering channels are active in MoB_2. Such a constraint could also suppress anharmonic effects in MoB_4 compared to MoB_2, resulting in a larger κ_{ph} for the former. Furthermore, since the σ_h symmetry is less efficient in MoB_4 (due to the presence of atoms away from the horizontal symmetry plane) in comparison to graphene, it is expected that the thermal conductivity of MoB_4 is less sensitive to the breaking of σ_h symmetry caused by the substrate. However, the actual reduction of κ_{ph} is also the result of the damping of ZA mode. This has a significant contribution to the suppression of thermal conductivity, which is the result of the interaction of 2D material with substrates [61,62] and must be evaluated on a case-by-case basis. Up to this point, we have discussed κ_{ph} for, in principle, infinite sample sizes [63]. To better understand the effects of sample size, the cumulative κ_{ph} as a function of the mean free path (MFP) at RT is plotted in Fig. 3 (b). The plot reveals that for both MoB_2 and MoB_4 the thermal conductivity is similar for sample sizes up to around 100 nm. From 100 nm to 200 nm, MoB_2 exhibits a small gain compared to MoB_4. Beyond 200 nm sample sizes, while κ_{ph} saturates for MoB_2, it dramatically increases for MoB_4. Moreover, the dashed lines in Fig. 3 (b) is corresponding to a fit extracted from $\kappa_{ph}(\Lambda \leq \Lambda_{\max}) = \frac{\kappa_{ph}}{1+\frac{\Lambda_0}{\Lambda_{\max}}}$ [36]. Our results manifest $\Lambda_0 = 4223$ (108) nm for MoB_4 (MoB_2), which can help follow decreasing of κ_{ph} with respect to the size of the nanocrystals. In addition, our calculations indicate that the scattering rate corresponding to isotopic impurities, Γ^{ext}, only possesses sensitive amounts in high phonon frequencies and, consequentially, show that neglecting isotopic effects can enhance κ_{ph} only about 9% at RT.

To better understand the underlying reason for the enhancement of κ_{ph} for MoB_4 versus MoB_2, in Fig. 4, we compare different quantities affecting κ_{ph}. A comparison between the relaxation times is shown in Fig. 4(a). We can see an overall relaxation time enhancement of MoB_4 compared to MoB_2 in the whole range of energies, particularly approximately two orders of magnitude enhancement for small phonon energies. Such stark differences between both cases mentioned above could be traced to the two other features, namely, a pure phononic band structure property, i.e., P_3 [36], and the level of anharmonicity. Fig. 4(b) indicates a larger P_3 for MoB_2 than MoB_4, which shows a larger scattering phase-space for MoB_2, resulting in a smaller τ.

To compare the amount of non-linearity, in Fig. 4(c), we plot the Grüneisen parameter corresponding to MoB_2 and MoB_4 as a function of phonon energies. Comparing γ for the two materials, we can see that γ of MoB_2 is overall larger than MoB_4. Another analogy for the amount of anharmonicity could be achieved by $\frac{\Gamma(\omega)}{WP_3(\omega)}$ (for the definition of WP_3 see Ref. [36]), as outlined in Fig. 4(d). The latter plot indicates a clear amplification of $\frac{\Gamma(\omega)}{WP_3(\omega)}$ for MoB_2 in contrast to that of MoB_4, which results in κ_{ph} improvement for the latter. Thus, in terms of the juxtaposition of MoB_4 and MoB_2, besides the larger sound velocities of MoB_4, the suppressed scattering space and the restrained anharmonic effects in MoB_4 result in an 8-fold improvement of the κ_{ph} of MoB_4 at RT.

Additionally, various studies have highlighted the significance of fourth-order phonon scatterings in a wide range of materials [25, 64–67]. Therefore, to examine the role of four-phonon scattering, following the approach of Ref. [65], we compared the weighted phase spaces WP_4 and WP_3 of MoB_4 as shown in Fig. 5 (for computational details see Ref. [68]). Our results reveal that the weighed phase space for WP_4 is at least two orders of magnitude smaller than that of WP_3, indicating a weak effect of fourth-order phonons on the scattering rate and lattice thermal transport.

4. Conclusion

In summary, we have studied the mechanical and thermal conductivity of a monolayer of MoB_4. Our calculations indicate that MoB_4 has a remarkable tensile strength with a Young's modulus of approximately 384 N/m, which is comparable to graphene and significantly larger than that of a single boron sheet and MoB_2. Our results also reveal a negative Grüneisen parameter for the ZA mode close to the zone center. However, unlike other well-known 2D materials such as graphene, germanene, and blue phosphorene, the total Grüneisen parameter is positive for MoB_4 above 66 K, resulting in a positive thermal expansion. Additionally, we calculated the thermal conductivity of MoB_4 and found it to be high, with a value of $\kappa_{ph} \simeq 461$ W/mK. Our findings also indicate that the contribution of the ZA mode to thermal conductivity is relatively small

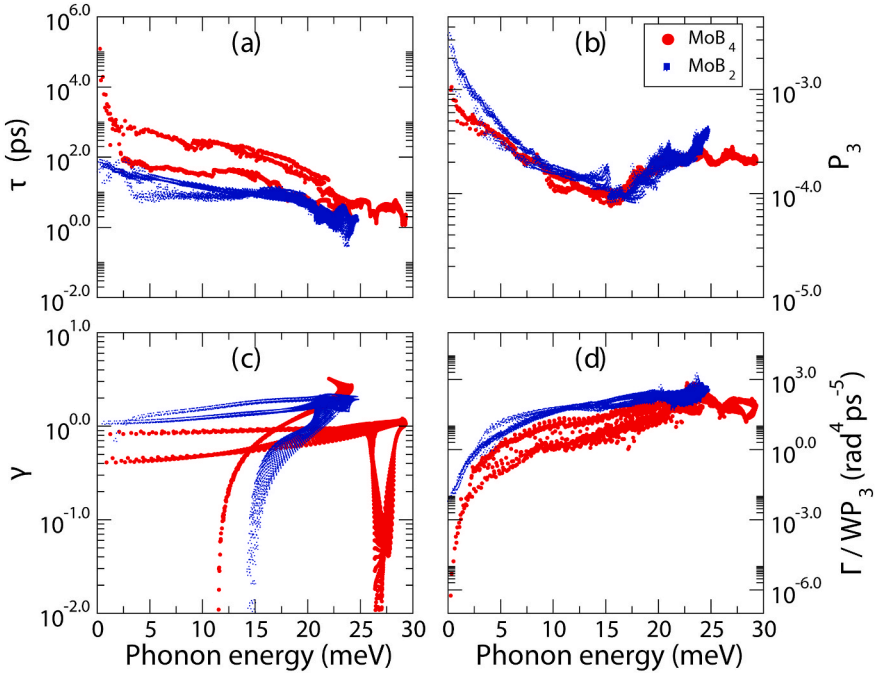

Fig. 4. (a) Relaxation time (τ), (b) allowed three-phonon phase space (P_3), (c) Grüneisen parameter (γ), and (d) anharmonic scattering rate divided by weighted phase space (WP_3) versus phonon energy for monolayer MoB_4 and MoB_2.

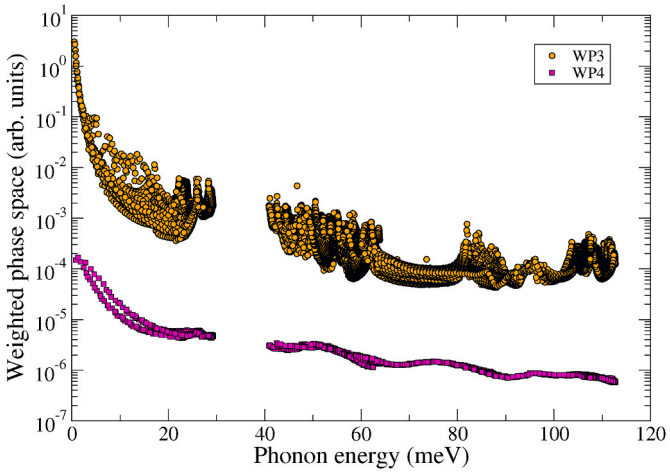

Fig. 5. Comparison of the weighted phase spaces WP_3 and WP_4 for a monolayer of MoB_4 at 300 K. The value of the scalebroad in ShengBTE is set to 1.0.

(35%) compared to that of graphene (75%). To analyze our results, we compared our findings for MoB_4 with those for MoB_2. For MoB_4, an enhanced group velocity of TA and LA modes in combination with a reduced scattering phase space and suppressed anharmonicity led to an 8X and 32X enhancement of thermal conductivity compared to MoB_2 and the single honeycomb boron sheet. This study motivates further research into the use of other transition metals with different boron allotropes to engineer materials with superior mechanical and thermal properties.

CRediT author statement

Mohammad Alidoosti: Investigation, Methodology, Software, Data curation, Formal analysis, Writing- Original draft preparation, **Shahram Yalameha**: Data curation, Software, Formal analysis, Validation, Writing- Reviewing and Editing. **Davoud Nasr Esfahani**: Supervision, Conceptualization, Validation, Formal analysis, Resources, Writing- Reviewing and Editing. **Daryoosh Vashaee**: Supervision, Resources, Validation, Formal analysis, Funding acquisition, Writing- Reviewing and Editing.

Declaration of competing interest

The authors declare the following financial interests/personal relationships which may be considered as potential competing interests: Daryoosh Vashaee reports financial support was provided by National Science Foundation.

Data availability

Data will be made available on request.

Acknowledgements

DV acknowledges the funding support by NSF under grant numbers ECCS-1711253 and CBET-2110603.

References

[1] J. Nagamatsu, N. Nakagawa, T. Muranaka, Y. Zenitani, J. Akimitsu, Superconductivity at 39 k in magnesium diboride, Nature 410 (6824) (2001) 63–64, https://doi.org/10.1038/35065039.
[2] G. Akopov, M. T. Yeung, R. B. Kaner, Rediscovering the crystal chemistry of borides, Adv. Mater. 29 (21) 1604506. doi:https://doi.org/10.1002/adma.201604506.
[3] S.-J. Gong, C. Gong, Y.-Y. Sun, W.-Y. Tong, C.-G. Duan, J.-H. Chu, X. Zhang, Electrically induced 2d half-metallic antiferromagnets and spin field effect transistors, Proc. Natl. Acad. Sci. 115 (34) (2018) 8511–8516, https://doi.org/10.1073/pnas.1715465115.
[4] C. Gu, Y. Liang, X. Zhou, J. Chen, D. Ma, J. Qin, W. Zhang, Q. Zhang, L.L. Daemen, Y. Zhao, S. Wang, Crystal structures and formation mechanisms of boron-rich tungsten borides, Phys. Rev. B 104 (2021): 014110, https://doi.org/10.1103/PhysRevB.104.014110.
[5] B. Albert, H. Hillebrecht, Boron: Elementary challenge for experimenters and theoreticians, Angew. Chem. Int. Ed. 48 (46) 8640–8668. doi:https://doi.org/10.1002/anie.200903246.
[6] Q. Gu, G. Krauss, W. Steurer, Transition metal borides: Superhard versus ultra-incompressible, Adv. Mater. 20 (19) 3620–3626. doi:https://doi.org/10.1002/adma.200703025.
[7] M. Wang, Y. Li, T. Cui, Y. Ma, G. Zou, Origin of hardness in WB_4 and its implications for ReB_4, TaB_4, MoB_4, TcB_4, and OsB_4, Appl. Phys. Lett. 93 (10) (2008): 101905, https://doi.org/10.1063/1.2977760.
[8] H. Tang, X. Gao, J. Zhang, B. Gao, W. Zhou, B. Yan, X. Li, Q. Zhang, S. Peng, D. Huang, L. Zhang, X. Yuan, B. Wan, C. Peng, L. Wu, D. Zhang, H. Liu, L. Gu, F. Gao, T. Irifune, R. Ahuja, H.-K. Mao, H. Gou, Boron-rich molybdenum boride with unusual short-range vacancy ordering, anisotropic hardness, and superconductivity, Chem. Mater. 32 (1) (2020) 459–467, https://doi.org/10.1021/acs.chemmater.9b04052.
[9] M. Zhang, H. Yan, Q. Wei, B. Zheng, Reinvestigation of mechanical properties and shear-induced atomic deformation of tetragonal superhard semiconducting OsB_4, J. Phys. Chem. C 121 (11) (2017) 6290–6299, https://doi.org/10.1021/acs.jpcc.6b12992.
[10] M. Zhang, H. Wang, H. Wang, T. Cui, Y. Ma, Structural modifications and mechanical properties of molybdenum borides from first principles, J. Phys. Chem. C 114 (14) (2010) 6722–6725, https://doi.org/10.1021/jp100225c.
[11] S. Chahal, P. Ranjan, M. Motlag, S. S. R. K. C. Yamijala, D. J. Late, E. H. S. Sadki, G. J. Cheng, P. Kumar, Borophene via micromechanical exfoliation, Adv. Mater. 33 (34) 2102039. doi:https://doi.org/10.1002/adma.202102039.
[12] A.J. Mannix, X.-F. Zhou, B. Kiraly, J.D. Wood, D. Alducin, B.D. Myers, X. Liu, B. L. Fisher, U. Santiago, J.R. Guest, M.J. Yacaman, A. Ponce, A.R. Oganov, M. C. Hersam, N.P. Guisinger, Synthesis of borophenes: anisotropic, two-dimensional boron polymorphs, Science 350 (6267) (2015) 1513–1516, https://doi.org/10.1126/science.aad1080.
[13] Z. Zhang, E.S. Penev, B.I. Yakobson, Two-dimensional materials: polyphony in b flat, Nat. Chem. 8 (6) (2016) 525–527, https://doi.org/10.1038/nchem.2521.
[14] Y. Yin, D. Li, Y. Hu, G. Ding, H. Zhou, G. Zhang, Phonon stability and phonon transport of graphene-like borophene, Nanotechnology 31 (31) (2020) 315709, https://doi.org/10.1088/1361-6528/ab824c.
[15] S.-Y. Xie, X.-B. Li, W.Q. Tian, N.-K. Chen, X.-L. Zhang, Y. Wang, S. Zhang, H.-B. Sun, First-principles calculations of a robust two-dimensional boron honeycomb sandwiching a triangular molybdenum layer, Phys. Rev. B 90 (2014): 035447, https://doi.org/10.1103/PhysRevB.90.035447.
[16] C. Zhang, Y. Jiao, F. Ma, S. Bottle, M. Zhao, Z. Chen, A. Du, Predicting a graphene-like WB_4 nanosheet with a double Dirac cone, an ultra-high Fermi velocity and significant gap opening by spin–orbit coupling, Phys. Chem. Chem. Phys. 19 (2017) 5449–5453, https://doi.org/10.1039/C7CP00157F.
[17] T. Kondo, Recent progress in boron nanomaterials, Sci. Technol. Adv. Mater. 18 (1) (2017) 780–804, https://doi.org/10.1080/14686996.2017.1379856, pMID: 29152014.
[18] F. Ma, Y. Jiao, G. Gao, Y. Gu, A. Bilic, Z. Chen, A. Du, Graphene-like two-dimensional ionic boron with double Dirac cones at ambient condition, Nano Lett. 16 (5) (2016) 3022–3028, https://doi.org/10.1021/acs.nanolett.5b05292, pMID: 27050491.
[19] H. Gunda, L.E. Klebanoff, P.A. Sharma, A.K. Varma, V. Dolia, K. Jasuja, V. Stavila, Progress, challenges, and opportunities in the synthesis, characterization, and application of metal-boride-derived two-dimensional nanostructures, ACS Mater. Lett. 3 (5) (2021) 535–556, https://doi.org/10.1021/acsmaterialslett.1c00086.
[20] A. Lopez-Bezanilla, Interplay between p- and d- orbitals yields multiple Dirac states in one- and two-dimensional CrB_4, 2D Mater. 5 (3) (2018): 035041, https://doi.org/10.1088/2053-1583/aac9f9.
[21] A. Lopez-Bezanilla, Twelve inequivalent Dirac cones in two-dimensional ZrB_2, Phys. Rev. Mater. 2 (2018): 011002, https://doi.org/10.1103/PhysRevMaterials.2.011002.
[22] Q. Cai, E. Janzen, J.H. Edgar, W. Gan, S. Zhang, E.J.G. Santos, L.H. Li, Isotope effect on the thermal expansion coefficient of atomically thin boron nitride, 2D Mater. 8 (3) (2021): 034006, https://doi.org/10.1088/2053-1583/ac0730.
[23] Y. Hu, Y. Yin, S. Li, H. Zhou, D. Li, G. Zhang, Three-fold enhancement of in-plane thermal conductivity of borophene through metallic atom intercalation, Nano Lett. 20 (10) (2020) 7619–7626, https://doi.org/10.1021/acs.nanolett.0c03135, pMID: 32852213.
[24] Y. Hu, Y. Yin, G. Ding, J. Liu, H. Zhou, W. Feng, G. Zhang, D. Li, High thermal conductivity in covalently bonded bi-layer honeycomb boron arsenide, Mater. Today Phys. 17 (2021): 100346, https://doi.org/10.1016/j.mtphys.2021.100346.
[25] C. Yu, Y. Hu, J. He, S. Lu, D. Li, J. Chen, Strong four-phonon scattering in monolayer and hydrogenated bilayer BAs with horizontal mirror symmetry, Appl. Phys. Lett. 120 (13) (2022): 132201, https://doi.org/10.1063/5.0086608.
[26] L. Lindsay, D.A. Broido, N. Mingo, Flexural phonons and thermal transport in graphene, Phys. Rev. B 82 (2010): 115427, https://doi.org/10.1103/PhysRevB.82.115427.
[27] G. Fugallo, A. Cepellotti, L. Paulatto, M. Lazzeri, N. Marzari, F. Mauri, Thermal conductivity of graphene and graphite: collective excitations and mean free paths, Nano Lett. 14 (11) (2014) 6109–6114, https://doi.org/10.1021/nl502059f, pMID: 25343716.

[28] S. Lu, Y. Ouyang, C. Yu, P. Jiang, J. He, J. Chen, Tunable phononic thermal transport in two-dimensional C_6CaC_6 via guest atom intercalation, J. Appl. Phys. 129 (22) (2021): 225106, https://doi.org/10.1063/5.0051259 doi:10.1063/5.0051259 10.1063/5.0051259.

[29] S. Lu, W. Ren, J. He, C. Yu, P. Jiang, J. Chen, Enhancement of the lattice thermal conductivity of two-dimensional functionalized mxenes by inversion symmetry breaking, Phys. Rev. B 105 (2022): 165301, https://doi.org/10.1103/PhysRevB.105.165301, 10.1103/PhysRevB.105.165301.

[30] Y. An, S. Gong, Y. Hou, J. Li, R. Wu, Z. Jiao, T. Wang, J. Jiao, MoB_2: a new multifunctional transition metal diboride monolayer, J. Phys. Condens. Matter 32 (5) (2019): 055503, https://doi.org/10.1088/1361-648X/ab4e6e.

[31] P. Giannozzi, S. Baroni, N. Bonini, M. Calandra, R. Car, C. Cavazzoni, D. Ceresoli, G.L. Chiarotti, M. Cococcioni, I. Dabo, A.D. Corso, S. de Gironcoli, S. Fabris, G. Fratesi, R. Gebauer, U. Gerstmann, C. Gougoussis, A. Kokalj, M. Lazzeri, L. Martin-Samos, N. Marzari, F. Mauri, R. Mazzarello, S. Paolini, A. Pasquarello, L. Paulatto, C. Sbraccia, S. Scandolo, G. Sclauzero, A.P. Seitsonen, A. Smogunov, P. Umari, R.M. Wentzcovitch, Quantum espresso: a modular and open-source software project for quantum simulations of materials, J. Phys. Condens. Matter 21 (39) (2009) 395502, https://doi.org/10.1088/0953-8984/21/39/395502.

[32] J.P. Perdew, K. Burke, M. Ernzerhof, Generalized gradient approximation made simple, Phys. Rev. Lett. 77 (1996) 3865–3868, https://doi.org/10.1103/PhysRevLett.77.3865.

[33] H.J. Monkhorst, J.D. Pack, Special points for brillouin-zone integrations, Phys. Rev. B 13 (1976) 5188–5192, https://doi.org/10.1103/PhysRevB.13.5188.

[34] S. Baroni, S. de Gironcoli, A. Dal Corso, P. Giannozzi, Phonons and related crystal properties from density-functional perturbation theory, Rev. Mod. Phys. 73 (2001) 515–562, https://doi.org/10.1103/RevModPhys.73.515.

[35] More details reveal that considering 3^{rd}IFCs up to the seventh shell of neighbors can alter κ_{ph} less than 3% at room temperature.

[36] Shengbte, A solver of the Boltzmann transport equation for phonons, Comput. Phys. Commun. 185 (6) (2014) 1747–1758, https://doi.org/10.1016/j.cpc.2014.02.015.

[37] W. Li, N. Mingo, L. Lindsay, D.A. Broido, D.A. Stewart, N.A. Katcho, Thermal conductivity of diamond nanowires from first principles, Phys. Rev. B 85 (2012): 195436, https://doi.org/10.1103/PhysRevB.85.195436.

[38] W. Li, L. Lindsay, D.A. Broido, D.A. Stewart, N. Mingo, Thermal conductivity of bulk and nanowire $Mg_2Si_xSn_{1-x}$ alloys from first principles, Phys. Rev. B 86 (2012): 174307, https://doi.org/10.1103/PhysRevB.86.174307.

[39] N. Mounet, N. Marzari, First-principles determination of the structural, vibrational and thermodynamic properties of diamond, graphite, and derivatives, Phys. Rev. B 71 (20) (2005) 205214, https://doi.org/10.1103/PhysRevB.71.205214.

[40] J. Zhou, R. Huang, Internal lattice relaxation of single-layer graphene under in-plane deformation, J. Mech. Phys. Solid. 56 (4) (2008) 1609–1623, https://doi.org/10.1016/j.jmps.2007.07.013.

[41] M. Jamal, M. Bilal, I. Ahmad, S. Jalali-Asadabadi, Irelast package, J. Alloys Compd. 735 (2018) 569–579, https://doi.org/10.1016/j.jallcom.2017.10.139.

[42] K.-A.N. Duerloo, M.T. Ong, E.J. Reed, Intrinsic piezoelectricity in two-dimensional materials, J. Phys. Chem. Lett. 3 (19) (2012) 2871–2876, https://doi.org/10.1021/jz3012436.

[43] P. Blaha, K. Schwarz, F. Tran, R. Laskowski, G.K.H. Madsen, L.D. Marks, Wien2k: an apw+lo program for calculating the properties of solids, J. Chem. Phys. 152 (7) (2020): 074101, https://doi.org/10.1063/1.5143061.

[44] S. Yalameha, Z. Nourbakhsh, D. Vashaee, Elatools: a tool for analyzing anisotropic elastic properties of the 2d and 3d materials, Comput. Phys. Commun. 271 (2022) 108195, https://doi.org/10.1016/j.cpc.2021.108195.

[45] A.O. de-la Roza, M. Blanco, A.M. Pendás, V. Luaña, Critic: a new program for the topological analysis of solid-state electron densities, Comput. Phys. Commun. 180 (1) (2009) 157–166, https://doi.org/10.1016/j.cpc.2008.07.018.

[46] A. Otero-de-la Roza, Finding critical points and reconstruction of electron densities on grids, J. Chem. Phys. 156 (22) (2022): 224116, https://doi.org/10.1063/5.0090232.

[47] J. Wang, S. Yip, S.R. Phillpot, D. Wolf, Crystal instabilities at finite strain, Phys. Rev. Lett. 71 (1993) 4182–4185, https://doi.org/10.1103/PhysRevLett.71.4182.

[48] H. Wang, X. Li, P. Li, J. Yang, phosphorene: a two dimensional material with a highly negative Poisson's ratio, Nanoscale 9 (2017) 850–855, https://doi.org/10.1039/C6NR08550D.

[49] X. Wei, B. Fragneaud, C.A. Marianetti, J.W. Kysar, Nonlinear elastic behavior of graphene: ab initio calculations to continuum description, Phys. Rev. B 80 (2009): 205407, https://doi.org/10.1103/PhysRevB.80.205407.

[50] Z. Wang, T.-Y. Lü, H.-Q. Wang, Y.P. Feng, J.-C. Zheng, High anisotropy of fully hydrogenated borophene, Phys. Chem. Chem. Phys. 18 (2016) 31424–31430, https://doi.org/10.1039/C6CP06164H.

[51] Z.-Q. Wang, T.-Y. Lü, H.-Q. Wang, Y.P. Feng, J.-C. Zheng, Band gap opening in 8-pmmn borophene by hydrogenation, ACS Appl. Electron. Mater. 1 (5) (2019) 667–674, https://doi.org/10.1021/acsaelm.9b00017.

[52] S. Zhang, J. Zhou, Q. Wang, X. Chen, Y. Kawazoe, P. Jena, Penta-graphene: A new carbon allotrope, Radioelectron. Nanosyst. Info. Technol. 112 (8) (2015) 2372–2377, https://doi.org/10.1073/pnas.1416591112.

[53] Z. Zhuo, X. Wu, J. Yang, Me-graphene: a graphene allotrope with near zero Poisson's ratio, sizeable band gap, and high carrier mobility, Nanoscale 12 (2020) 19359–19366, https://doi.org/10.1039/D0NR03869E.

[54] X.-J. Ge, K.-L. Yao, J.-T. Lü, Comparative study of phonon spectrum and thermal expansion of graphene, silicene, germanene, and blue phosphorene, Phys. Rev. B 94 (2016): 165433, https://doi.org/10.1103/PhysRevB.94.165433.

[55] H. Xiao, W. Cao, T. Ouyang, S. Guo, C. He, J. Zhong, Lattice thermal conductivity of borophene from first principle calculation, Sci. Rep. 7 (1) (2017) 1–8, https://doi.org/10.1038/srep45986.

[56] Y. Yin, Y. Hu, S. Li, G. Ding, S. Wang, D. Li, G. Zhang, Abnormal thermal conductivity enhancement in covalently bonded bilayer borophene allotrope, Nano Res 15 (4) (2022) 3818–3824, https://doi.org/10.1007/s12274-021-3921-y.

[57] J. He, Y. Ouyang, C. Yu, P. Jiang, W. Ren, J. Chen, Lattice thermal conductivity of β_{12} and χ_3 borophene, Chin. Phys. B 29 (12) (2020): 126503, https://doi.org/10.1088/1674-1056/abbbe6.

[58] L. Lindsay, D.A. Broido, N. Mingo, Flexural phonons and thermal transport in multilayer graphene and graphite, Phys. Rev. B 83 (2011): 235428, https://doi.org/10.1103/PhysRevB.83.235428.

[59] M. Alidoosti, D.N. Esfahani, R. Asgari, σ_h symmetry and electron-phonon interaction in two-dimensional crystalline systems, Phys. Rev. B 106 (2022): 045301, https://doi.org/10.1103/PhysRevB.106.045301.

[60] Y. Kuang, L. Lindsay, S. Shi, X. Wang, B. Huang, Thermal conductivity of graphene mediated by strain and size, International Journal of Heat and Mass Transfer 101 (2016) 772–778, https://doi.org/10.1016/j.ijheatmasstransfer.2016.05.072.

[61] Z. Zhang, S. Hu, J. Chen, B. Li, Hexagonal boron nitride: a promising substrate for graphene with high heat dissipation, Nanotechnology 28 (22) (2017): 225704, https://doi.org/10.1088/1361-6528/aa6e49, 10.1088/1361-6528/aa6e49.

[62] J. Chen, G. Zhang, B. Li, Substrate coupling suppresses size dependence of thermal conductivity in supported graphene, Nanoscale 5 (2013) 532–536, https://doi.org/10.1039/C2NR32949B, 10.1039/C2NR32949B.

[63] A.J. Minnich, J.A. Johnson, A.J. Schmidt, K. Esfarjani, M.S. Dresselhaus, K. A. Nelson, G. Chen, Thermal conductivity spectroscopy technique to measure phonon mean free paths, Phys. Rev. Lett. 107 (2011): 095901, https://doi.org/10.1103/PhysRevLett.107.095901.

[64] J. Chen, J. He, D. Pan, X. Wang, N. Yang, J. Zhu, S.A. Yang, G. Zhang, Emerging theory and phenomena in thermal conduction: a selective review, Sci. China Phys. Mech. Astron. 65 (11) (2022), https://doi.org/10.1007/s11433-022-1952-3.

[65] Z. Han, X. Yang, W. Li, T. Feng, X. Ruan, Fourphonon: an extension module to shengbte for computing four-phonon scattering rates and thermal conductivity, Comput. Phys. Commun. 270 (2022): 108179, 10.1016/j.cpc.2021.108179, https://www.sciencedirect.com/science/article/pii/S0010465521002915.

[66] T. Feng, X. Ruan, Quantum mechanical prediction of four-phonon scattering rates and reduced thermal conductivity of solids, Phys. Rev. B 93 (2016): 045202, https://doi.org/10.1103/PhysRevB.93.045202.

[67] T. Feng, L. Lindsay, X. Ruan, Four-phonon scattering significantly reduces intrinsic thermal conductivity of solids, Phys. Rev. B 96 (2017) 161201, https://doi.org/10.1103/PhysRevB.96.161201.

[68] To calculate fourth-order IFCs up to second nearest neighbors, 1256 distorted supercells ($5 \times 5 \times 1$ including 125 atoms) were used. Then, we calculated the four-phonon scattering phase space and compared it with that of the three-phonon phase space. Although, the main calculation in the manuscript has been calculated by **q**-mesh ($160 \times 160 \times 1$), almost converged results (For WP_4) were achieved by adopting q-mesh ($50 \times 50 \times 1$).